

The Current State of Reconstruction Technologies for 3D X-ray Microscopy including Algorithmic Innovation for AI-based Recovery

April 26, 10:00am - 11:00am EDT

Many properties can only be fully understood in 3D, such as porosity and tortuosity in porous materials, network connection maps in neuroscience, or mechanical properties in 3D additively manufactured structures. X-ray microscopy provides a unique method to image samples non-destructively in 3D across a wide range of materials and life sciences.

Watch this session during the WAS Virtual Conference:



Nicolas Guenichault, Ph.D.



Dr. Stephen T. Kelly, Ph.D.

[Register Now](#)

This talk is sponsored by



Additively Manufactured Polarization Insensitive Broadband Transmissive Metasurfaces for Arbitrary Polarization Conversion and Wavefront Shaping

Jianfeng Zhu, Yang Yang,* Jiexin Lai, and Jaim Nulman

Arbitrarily manipulating the polarization and wavefront of electromagnetic waves using ultrathin and highly efficient devices is desirable for many systems. Ultrathin broadband polarization-insensitive transmissive metasurfaces, which can achieve the same polarization conversion and wavefront shaping for arbitrary linearly polarized incident waves, are proposed. The meta-atom is composed of a transmitting antenna and a receiving antenna with a group of phase delay lines connecting them. The rotation of the transmitting antenna introduces the polarization conversion, and the different lengths of the transmission lines provide $[-\pi, \pi]$ phase shift for wavefront shaping. Both the polarization conversion and wavefront shaping functions are polarization insensitive. Differential feeding is applied to both the transmitting and the receiving patch antennas to improve the transmission efficiency. The prototypes are conveniently printed by using the additive manufacturing technique. Two polarization-insensitive metasurfaces are designed and measured to demonstrate. One of them produces vortex beams with 90° polarization conversion, and the other achieves anomalous refraction with 45° polarization conversion.

1. Introduction


Metasurface (MS), composed of electrical-small meta-atoms arranged on a 2D planar surface or interface, offers a platform to manipulate the electromagnetic (EM) wave at will.^[1–3] The most distinguishing feature of a MS is its flexible ability to control the amplitude, phase, and polarization of the wavefront, leading to the applications such as flat meta-lens,^[4–9] reflectarrays,^[10–12] frequency selective surfaces,^[13–15] vortex beam

generations,^[16–20] and holograms.^[21–23] For example, digital and programmable MSs were demonstrated in the microwave region.^[24–26] The wavefront and polarization can be dynamically controlled, showing great potential for future intelligent systems. The spin decoupled multi-channel devices were proposed for polarization multiplexed systems by combining the geometric and dynamic phases.^[27–29] The concept of multi-channel orbital angular momentum (OAM) multiplexing and demultiplexing was demonstrated using single-layer MS in optical regions, leading to high-speed and large-capacity optical communications.^[30] Broadband transmission-type spin decoupled dielectric MS combining the dynamic phase and geometric phase was proposed in the terahertz regime.^[31] By using multiplexed meta-atoms, the MS can also convert arbitrary linearly polarized waves to two different linearly polarized waves with

nearly equal strength and asymmetric angles, which opens new avenues for efficient polarization-multiplexed THz systems. In the meantime, non-interleaved polarization-insensitive MSs for efficient wavefront shaping are also widely investigated. For instance, broadband polarization-insensitive 3D conformal MS cloaks were demonstrated to conceal targets under polarization-scanning detections.^[32,33] By exploiting cross linear polarization dynamic and geometric phases, the polarization and the intensity of the scattered EM-wave can be reconstructed as the scattering wavefront deflected from the flat ground at any polarization state. Highly efficient dielectric resonant-based MSs are demonstrated in the optical region, with identical hologram images,^[34] vortex beams,^[35] and focusing^[36] observed under different linear polarization. In the microwave region, polarization-insensitive transmissive MSs are also demonstrated to flexibly manipulate the wavefront, which is usually achieved by cascading resonant cells in several laminates.^[37,38] However, The MSs cannot perform polarization conversion because the meta-atoms are isotropic. For state-of-the-art MSs that achieve both polarization conversion and wavefront shaping, the polarization conversion feature usually depends on the polarization of the input. For example, an all-dielectric MS for simultaneously realizing polarization rotation and wavefront shaping was demonstrated in visible light.^[39] Because the cross-polarization conversion is achieved based on the principle of the half-wave

J. Zhu, Y. Yang, J. Lai
School of Electrical and Data Engineering
University of Technology Sydney
Tech Lab, Sydney, NSW 2019, Australia
E-mail: yang.yang.au@ieee.org

J. Nulman
Nano Dimension USA
13898 NW 4th St, Suite 315, Sunrise, FL 33325, USA

 The ORCID identification number(s) for the author(s) of this article can be found under <https://doi.org/10.1002/adom.202200928>.

© 2022 The Authors. Advanced Optical Materials published by Wiley-VCH GmbH. This is an open access article under the terms of the Creative Commons Attribution License, which permits use, distribution and reproduction in any medium, provided the original work is properly cited.

DOI: 10.1002/adom.202200928

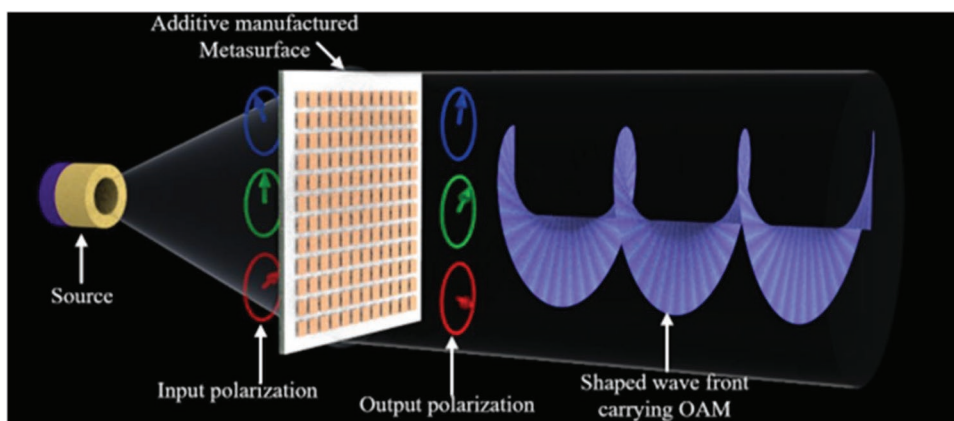


Figure 1. Additively manufactured polarization-insensitive MS for arbitrary polarization conversion and shaped wavefront carrying OAM. The blue, green, and red arrows represent different linearly polarized inputs and the corresponding outputs. The polarization conversion angle between the input and output states and the wavefront are fixed regardless of the polarization of linearly polarized input.

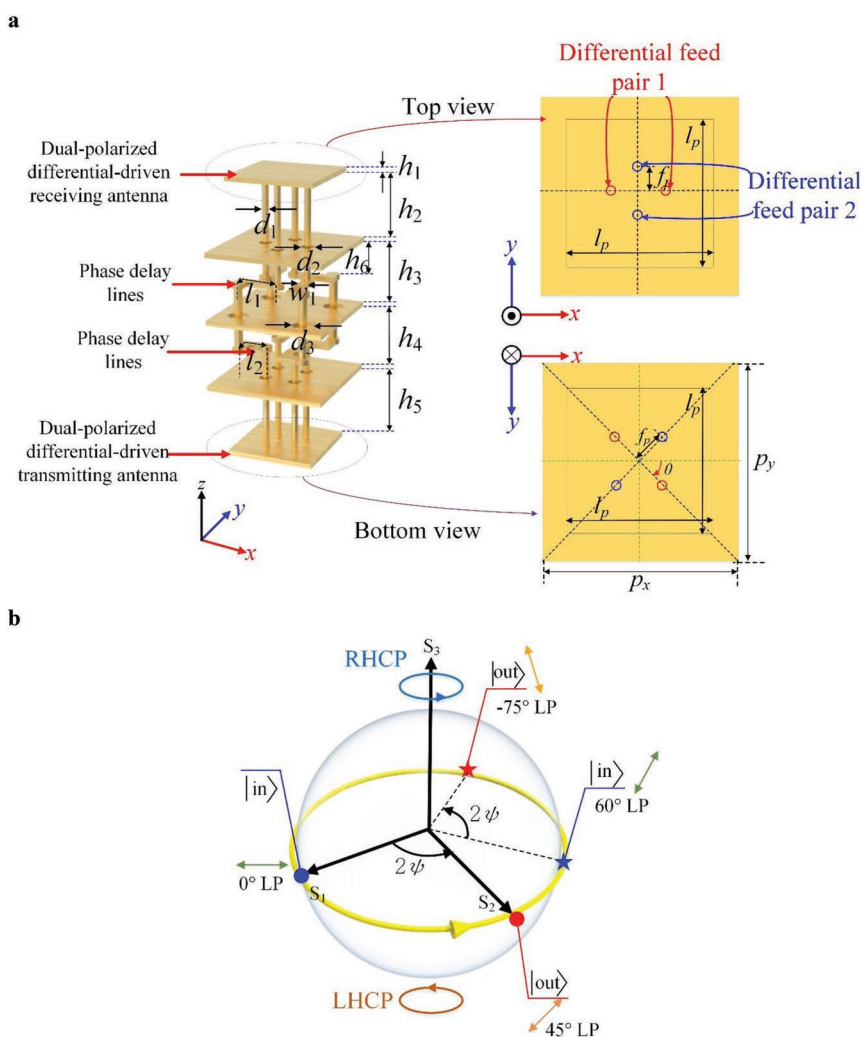


Figure 2. a) Configuration of the meta-atom. The bottom patch's feeding is rotated at an angle of θ compared with that of the top patch. ($h_1 = 0.035$ mm, $h_2 = 0.47$ mm, $h_3 = 0.435$ mm, $h_4 = 0.435$ mm, $h_5 = 0.47$ mm, $h_6 = 0.2$ mm, $p_x = 3.5$ mm, $p_y = 3.5$ mm, $d_1 = 0.2$ mm, $d_2 = 0.4$ mm, $d_3 = 0.6$ mm, $w_1 = 0.3$ mm; l_1 and l_2 represent the total lengths of the top and bottom phase delay lines, which are varied in the 3-bit meta-atoms.) b) Poincaré sphere. The meta-atom is circular birefringence, which induces a conversion of polarization states on the Poincaré sphere (along the yellow lines), with black axis S_3 as the rotation axis and the rotation angle determined by the retardance between the meta-atom's two eigen-polarization states (RHCP/LHCP).^[49] The azimuth angle 2ψ is constant between the input and output regardless of the location of the LP input on the equator.

plate (HWP), the cross-polarization conversion is achieved only when the input polarization is 45° compared with the fast axis of the HWP. Multi-channel polarization conversion and wavefront shaping all-dielectric MS was demonstrated in the Terahertz region.^[40] The output polarizations are RHCP and 45° linear polarization under x -polarized and y -polarized incident waves, respectively. To the author's knowledge, transmissive MSs with polarization conversion and wavefront control that are polarization insensitive are rarely reported.

In terms of fabrication, micro/nano-fabrication and printed circuit board (PCB) are commonly used techniques for fabricating MSs in optical and microwave regions. Different from these fabrication methods, additive manufacturing, also known as 3D printing, provides new possibilities for fabricating complex metamaterial structures with predefined optical, acoustic, and mechanical properties, many of which cannot be realized through conventional fabrication methods.^[41] For example, conformal carpet cloaks are demonstrated using additive manufacturing^[42] with a thermally programmable feature.^[43] Different kinds of gradient-index metamaterial lenses from acoustic to terahertz regions were demonstrated using fused deposition modeling or micro-stereolithography.^[44–47] Undoubtedly, the rise of additive manufacturing helps unlock the great potential of metamaterials, paving the way to the future high-efficient, multi-functional, and cost-effective intelligent systems.

This article proposes an additively manufactured ultrathin broadband polarization-insensitive transmissive MS, which achieves the same polarization conversion and wavefront shaping for any linearly polarized incident waves, as depicted in **Figure 1**. The meta-atom comprises a receiving antenna, a transmitting antenna, and a group of phase delay lines connecting them. Both the receiving and transmitting antennas are designed by dual-polarized patches, which can efficiently receive or transmit EM waves. The receiving and transmitting antennas are connected by using phase delay lines. $[-\pi, \pi]$ phase shifting can be achieved by conveniently adjusting the length of the phase delay line. Differential feeding is applied to both the transmitting and the receiving patch antenna. The

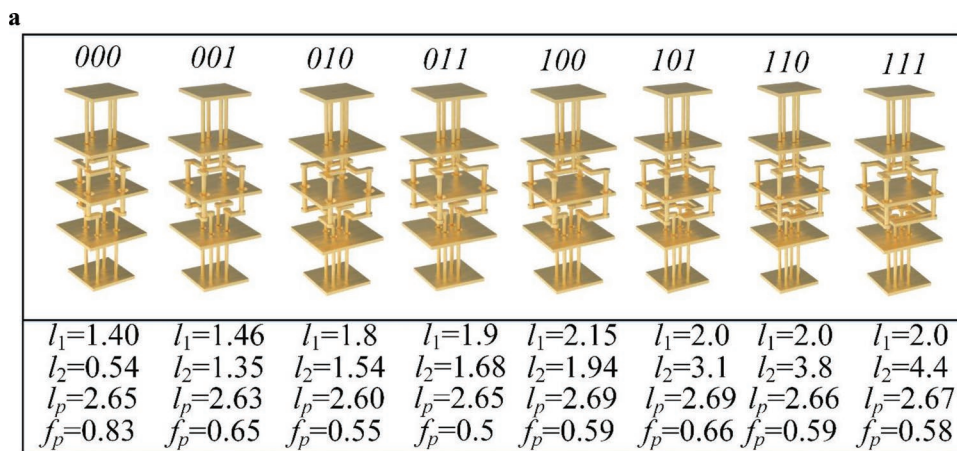
higher-order modes of the patch antenna can be avoided due to the inherent nature of the differential feeding. Hence, the MS can achieve high polarization conversion efficiency. The differential feeding port of the receiving antenna is fixed, while the differential feeding port of the transmitting antenna is rotated. The polarization conversion for the incident wave depends on the rotation angle of the feeding port of the transmitting antenna, and this polarization conversion is insensitive to the polarization of the LP input. Taking advantage of the advanced additive manufacturing technique, the MS prototypes are conveniently fabricated. Two polarization-insensitive MSs are simulated and measured for proof of concept. One achieves 90° polarization conversion with the shaped wavefront carrying OAM beams. The other achieves 45° polarization conversion with anomalous refraction.

2. Meta-Atom Design and Theoretical Analysis

The meta-atom consists of a dual-polarized differential-driven square patch at the top as the receiving antenna, a dual-polarized differential-driven square patch at the bottom as the transmitting antenna, and a group of phase delay lines connecting them, as depicted in **Figure 2a**. Ultraviolet (UV) curable acrylates ink is used as the dielectric layer with a dielectric constant of 2.8 and loss tangent of 0.013. The thickness of all conductive layers is $35 \mu\text{m}$ (h_1) to provide robust connections, which are printed using silver nanoparticle ink. The dielectric layer's primary function is to help support the multiple conductor layers. The seven conductor layers and the vias cannot be stacked in order without supporting material. In the meantime, the presence of the dielectric layer can help reduce the size of the unit cell since the size of the patch antenna depends on the dielectric wavelength. The unit cell period is only 0.35 free-space wavelength at 30 GHz. Two differential feed pairs arranged in the orthogonal directions are used to feed the patch antenna, as shown in **Figure 2a**. Note that compared with a single-ended dual-polarized patch antenna, the

Table 1. Comparison of state-of-the-art transmit-type metasurfaces for simultaneous polarization conversion and wavefront shaping.

Ref.	Frequency	Configuration	Polarization conversion	Wavefront shaping	Fabrication	
[39]	Visible (690 nm)	Dielectric block	Cross-polarization conversion/HWP (polarization insensitive)	Arbitrary (polarization insensitive)	Micro-fabrication	
[40]	THz (1.1 THz)	Interleaved dielectric block	x -polarization to RHCP; y -polarization to 45° LP (polarization sensitive)	Arbitrary (polarization insensitive)	Micro-fabrication	
[50]	THz (1.4 THz)	Multilayer FSS	Cross-polarization conversion (polarization sensitive)	Arbitrary (polarization sensitive)	Micro-fabrication	
[51]	Millimeter wave (30 GHz)	Multilayer FSS	Cross-polarization conversion (polarization sensitive)	Arbitrary (polarization sensitive)	PCB	
[52]	Millimeter wave (77 GHz)	Multilayer FSS	LP to CP/quarter-wave plate (polarization sensitive)	Arbitrary (polarization insensitive)	PCB	
[53]	Millimeter wave (30 GHz)	Dielectric block	LP to CP/quarter-wave plate (polarization sensitive)	Arbitrary (polarization insensitive)	Additive manufacturing	
This work	MS I	Millimeter wave (30 GHz)	Antenna-phase delay line-antenna	45° polarization conversion (polarization insensitive)	Arbitrary (polarization insensitive)	Additive manufacturing
	MS II	Millimeter wave (30 GHz)	Antenna-phase delay line-antenna	Cross-polarization conversion (polarization insensitive)	Arbitrary (polarization insensitive)	Additive manufacturing



Unit: mm

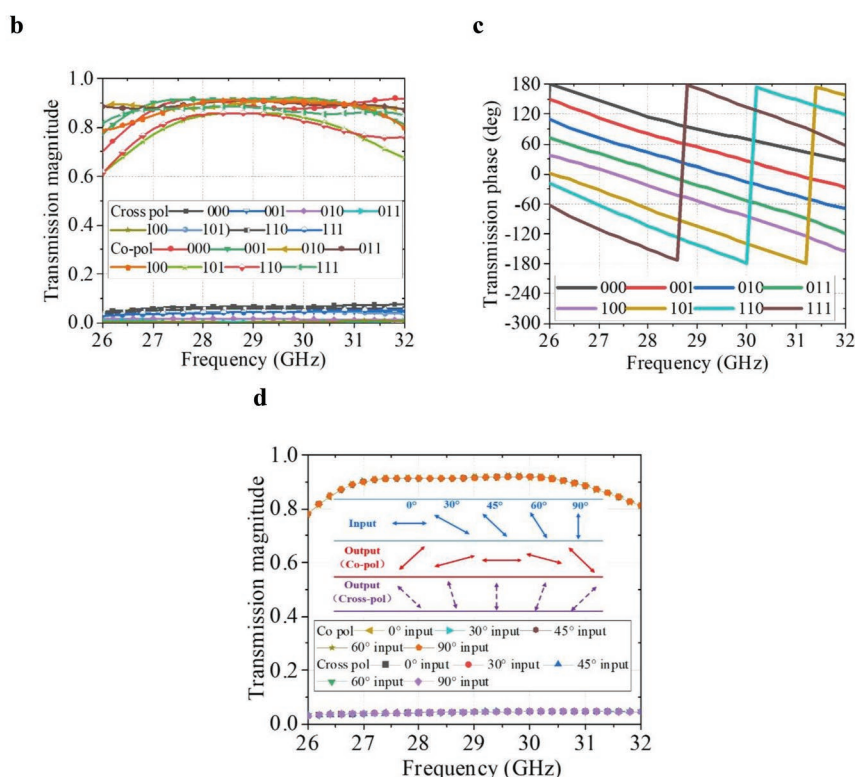


Figure 3. a) Configuration of the eight-level 45° polarization conversion meta-atoms. b) Transmission magnitude of the eight-level meta-atoms. c) Transmission phase of the eight-level meta-atoms. d) Transmission magnitude of the 001 element under different linearly polarized incident waves. For the 45° polarization conversion MS, the co-pol/cross-pol of the output is defined as the polarization that has $45^\circ/-45^\circ$ rotation compared with that of the input.

differentially-driven microstrip antenna introduces the cancellation mechanism, which suppresses higher-order modes to reduce the cross-polarization radiation.^[48] Therefore, the polarization conversion efficiency can be improved. Meta-atoms based on single-ended dual-polarized patch antenna are also simulated for comparison, see Figure S1, Supporting Information. The position of the differential feeding on the receiving side is fixed while the one on the transmitting side is rotated at an angle of θ , as shown in Figure 2a. In this way,

the output polarization will be rotated at an angle of θ for any linearly polarized incident wave.

The meta-atom's operating principles can be understood by using the Jones matrix. For an arbitrary linearly polarized incident wave, the input vectors of the electric field are expressed as

$$E^i = \begin{bmatrix} E^x \\ E^y \end{bmatrix} = \begin{bmatrix} \cos \alpha \\ \sin \alpha \end{bmatrix} \quad (1)$$

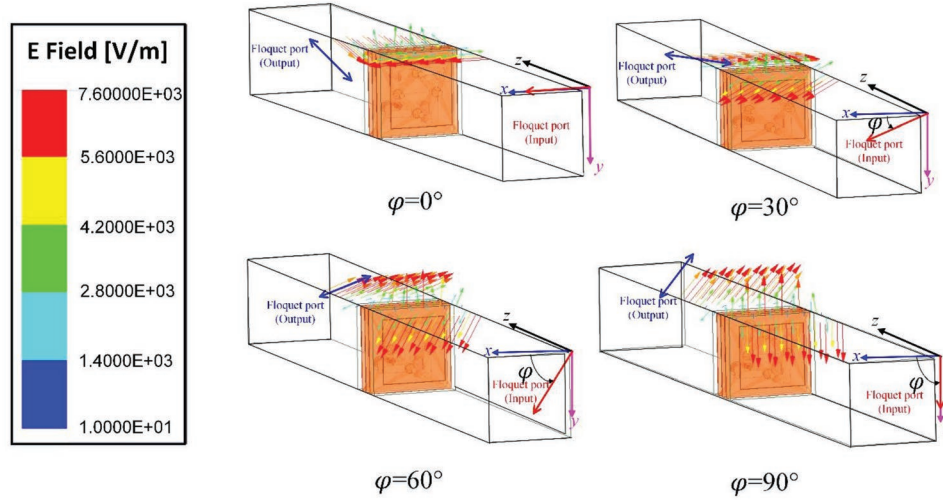


Figure 4. Simulated E-field distributions of the 45° polarization conversion meta-atom under different linearly polarized incident waves.

Assuming no loss, after being received by the dual-polarized receiving antenna and passing the phase delay line, the electric field can be written as

$$E^{i_1} = \begin{bmatrix} e^{-j\varphi} & 0 \\ 0 & e^{-j\varphi} \end{bmatrix} \times E^i \quad (2)$$

where φ represents the phase delay from the phase delay line. On the transmitting side, the feeding port is in-plane rotated at an angle of θ , the corresponding Jones matrix can be written as

$$J_1 = \begin{bmatrix} \cos\theta & \sin\theta \\ -\sin\theta & \cos\theta \end{bmatrix} \quad (3)$$

Then, the Jones vector of the output beam can be expressed as

$$E^{out} = J_1 \times E^{i_1} = \begin{bmatrix} \cos\theta & \sin\theta \\ -\sin\theta & \cos\theta \end{bmatrix} \times \begin{bmatrix} e^{-j\varphi} & 0 \\ 0 & e^{-j\varphi} \end{bmatrix} \times \begin{bmatrix} \cos\alpha \\ \sin\alpha \end{bmatrix} = \begin{bmatrix} \cos(\alpha - \theta) \\ \sin(\alpha - \theta) \end{bmatrix} \times e^{-j\varphi} \quad (4)$$

From Equations (4) and (1), the output E-field shows φ phase delay, and the polarization is rotated at an angle of θ compared to the input E-field. Similarly, considering the LHCP and RHCP input, the output E-field can be expressed as:

$$E^{out} = \begin{bmatrix} \cos\theta & \sin\theta \\ -\sin\theta & \cos\theta \end{bmatrix} \times \begin{bmatrix} e^{-j\varphi} & 0 \\ 0 & e^{-j\varphi} \end{bmatrix} \times \begin{bmatrix} 1 \\ i \end{bmatrix} = \begin{bmatrix} 1 \\ i \end{bmatrix} \times e^{-j\varphi} \times e^{j\theta} \quad \text{for LHCP} \quad (5a)$$

$$E^{out} = \begin{bmatrix} \cos\theta & \sin\theta \\ -\sin\theta & \cos\theta \end{bmatrix} \times \begin{bmatrix} e^{-j\varphi} & 0 \\ 0 & e^{-j\varphi} \end{bmatrix} \times \begin{bmatrix} 1 \\ -i \end{bmatrix} = \begin{bmatrix} 1 \\ -i \end{bmatrix} \times e^{-j\varphi} \times e^{-j\theta} \quad \text{for RHCP} \quad (5b)$$

It is seen that the meta-atom introduces an opposite phase delay of θ for the LHCP and RHCP input, but the circular polarization state remains unchanged after transmitting through the meta-atoms. Therefore, the LHCP and RHCP are two eigen-polarization states of the meta-atoms.^[49] The output polarization of any input polarization can be understood in the Poincaré sphere, Figure 2b depicts the Poincaré sphere of the 45° polarization conversion MS. Considering two arbitrary LP inputs, for example, 0° LP and 60° LP inputs, the output polarization will show the trajectory along the equator with the same azimuth angle 2ψ (ψ is 45°, equal to the rotation angle of the transmitting antenna of the meta-atom). Thus, the output polarization always maintains 45° polarization rotation compared with that of the input regardless of the location of the LP input on the equator. In addition, the ellipse angles of the input and output are the same, equal to zero. Meanwhile, the $[-\pi, \pi]$ phase shifting from phase delay lines is also insensitive to the input polarization. Therefore, the same polarization conversion and wavefront shaping can be maintained for arbitrary linearly polarized incident waves. This feature enables the MS to be different from the state-of-the-art MS, where the polarization conversion or wavefront shaping feature depends on a specific linear polarization state.^[39,40,50–57] A comparison of the state-of-the-art works is listed in **Table 1**.

Two sets of meta-atoms are demonstrated here for 45° and 90° polarization conversion and wavefront shaping. The configuration of the eight-level meta-atom (3-bit phase quantization) for achieving 45° polarization conversion is shown in **Figure 3a**. The lengths of the phase delay line of the 3-bit meta-atoms are different to provide phase shifting covering $[-\pi, \pi]$. When selecting the 3-bit meta-atoms, both transmission phase and transmission magnitudes need to be considered. First, we must ensure the phase difference between every adjacent meta-atom is around 45°. Therefore, the phase delay lines' lengths are swept in the simulation software Ansys HFSS for each meta-atom. The corresponding phase curves are compared, and the length of the phase delay line of each meta-atom is carefully selected, ensuring that the phase difference between the adjacent meta-atoms is around 45°. Second,

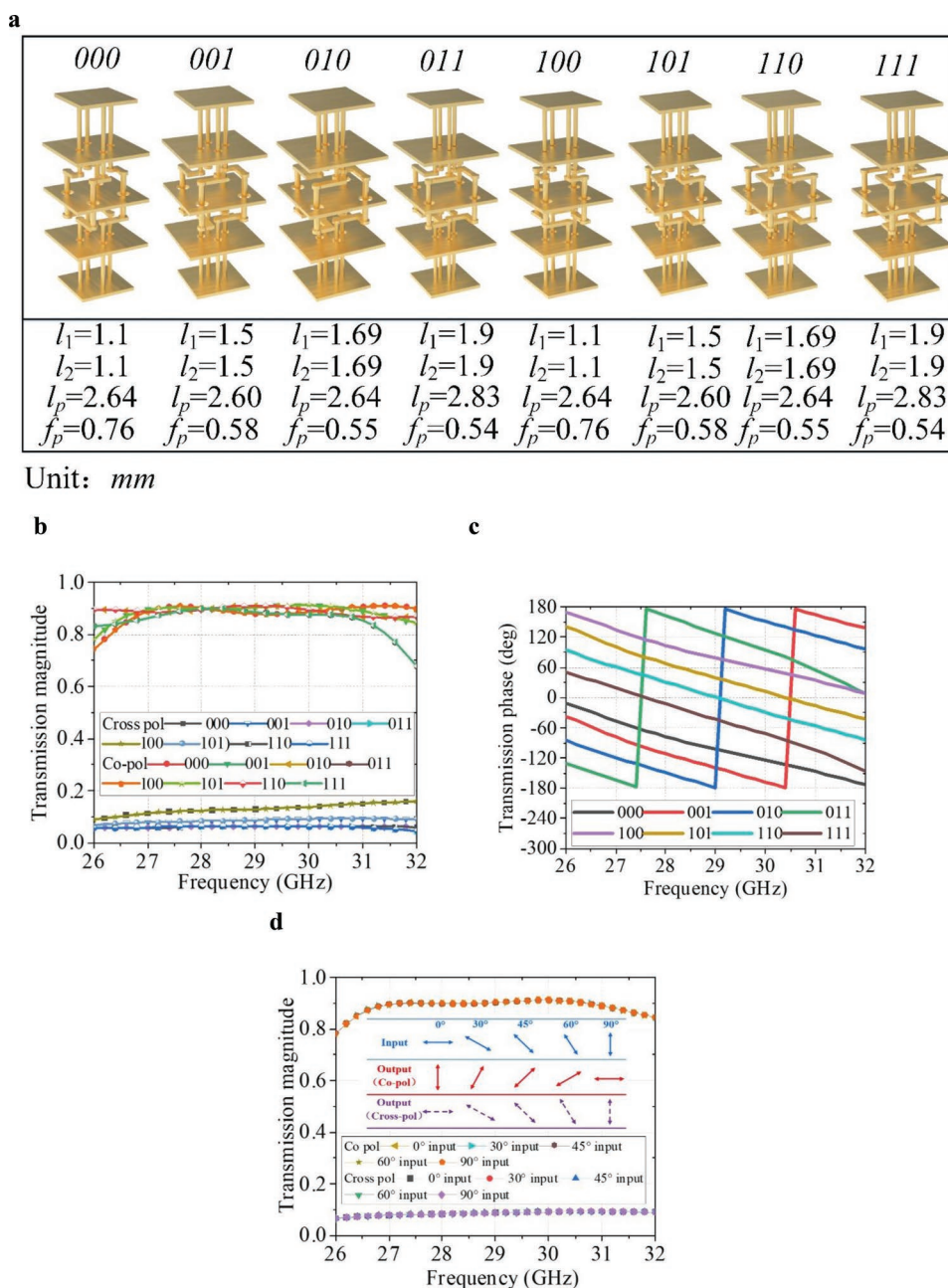


Figure 5. a) Configuration of the eight-level 90° polarization conversion meta-atoms. b) Transmission magnitude of the eight-level meta-atoms. c) Transmission phase of the eight-level meta-atoms. d) Transmission magnitude of the 001 element under different linearly polarized incident waves. For the 90° polarization conversion MS, the co-pol/cross-pol of the output is defined as the polarization that has 90°/0° rotation compared with that of the input.

high transmission magnitude is the other important aspect. Varying the length of the phase delay lines slightly affects the transmission magnitude. The transmission magnitude can be improved by further optimizing the patch's length (l_p) and the feeding port position (f_p) to match the phase delay lines. Therefore, the three parameters, that is, l_p , f_p , and the length of the phase delay lines, are further optimized in the HFSS optimization toolbox using the Quasi-Newton algorithm for each meta-atom, with the goal of the transmission magnitude

as high as possible and the phase difference between every adjacent meta-atom is around 45°.

The transmission magnitude and phase of 3-bit meta-atoms are given in Figures 3b,c, respectively. It is seen from Figure 3b that the transmission magnitude of the co-polarization is higher than 0.8, while the cross-polarization is less than 0.1. It is observed from Figure 3c that the phase delay lines provide a nearly linear phase response. Hence, the meta-atom can achieve wide operating bandwidth. Note that

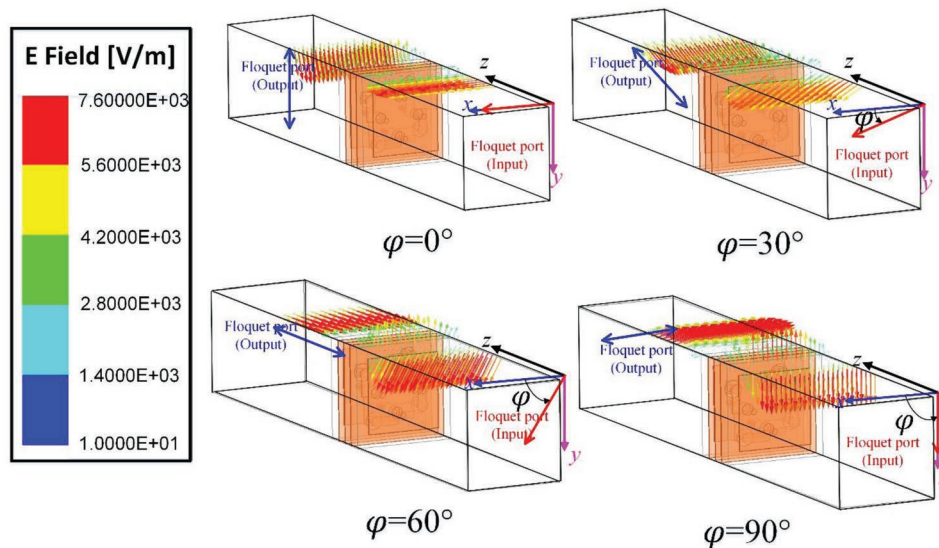


Figure 6. Simulated E-field distributions of the 90° polarization conversion meta-atom under different linearly polarized incident waves.

the dielectric material is relatively lossy, and some energy will dissipate in the material. Assuming no loss from the material, the transmission magnitude of co-polarization can be improved by 0.1 on average, see Figure S2, Supporting Information. The co- and cross-polarization transmission magnitudes under different linearly polarized incident waves are shown in Figure 3d. The output polarization is rotated at 45° for any linearly polarized incident wave, and the transmission magnitude curves are nearly the same for different incident waves. To better illustrate the function, the simulated vector E-field distributions for the meta-atom under 0°, 30°, 60°, and

90° linearly polarized incident waves are given in **Figure 4**. The output polarization is observed to be rotated by 45° compared with the input polarization.

The configuration of the 3-bit meta-atom for achieving 90° polarization conversion is shown in **Figure 5a**. Note that the length of the delay line of 100, 101, 110, and 111 elements are the same as 000, 001, 010, and 100 elements, respectively. Nevertheless, the position of the feeding ports on the transmitting side between them is mirror symmetry to achieve 180° phase shifting. The transmission magnitudes and phase are given in Figures 5b,c, respectively. It is seen in Figure 5b

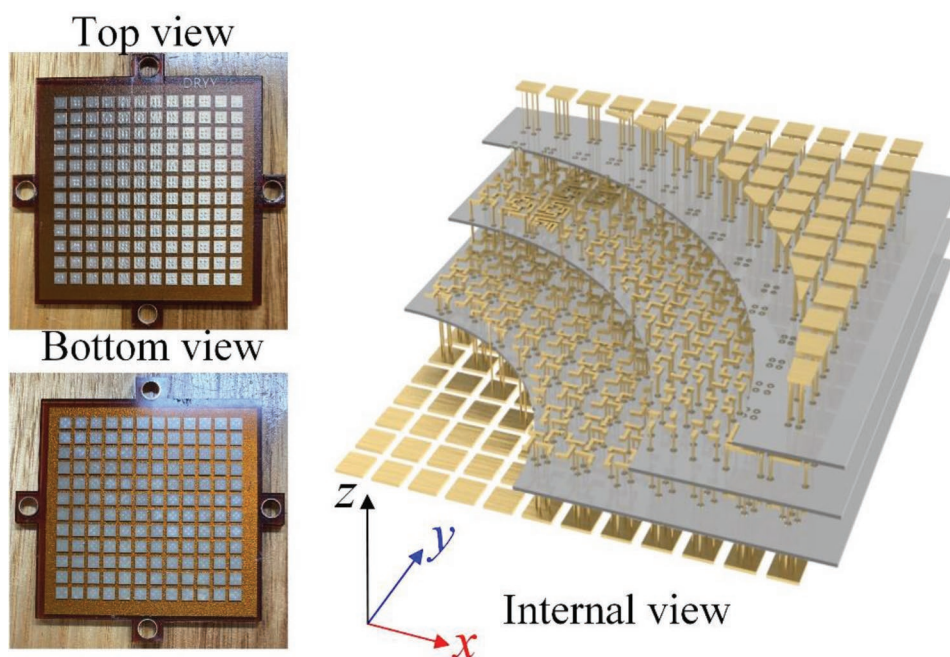


Figure 7. Prototype of the MS: the left images show the top view and bottom view of the additively manufactured MS. The right image shows the internal view of the MS model.

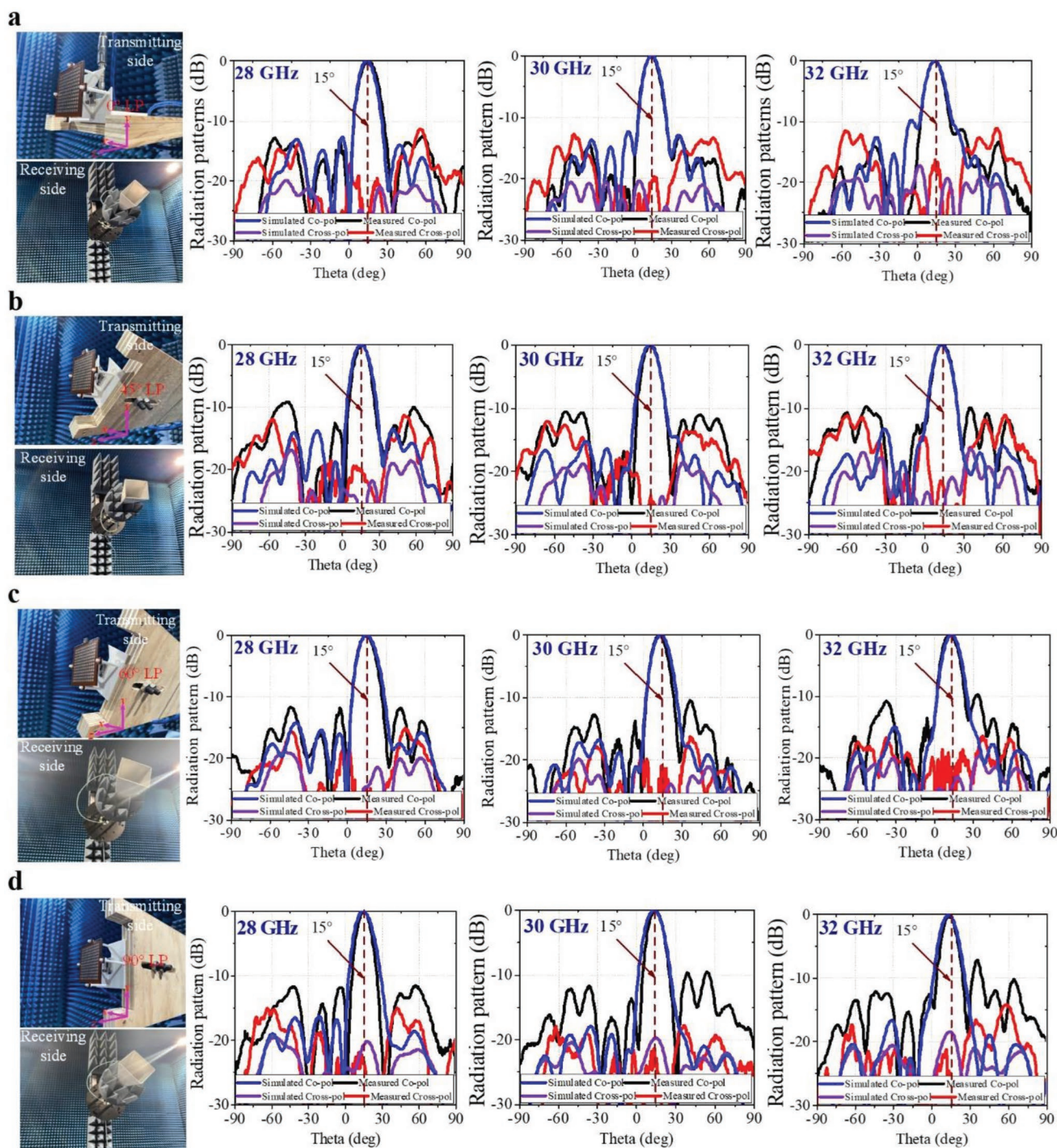


Figure 8. Assembling view during measurement and the far-field radiation patterns at 28 GHz, 30 GHz, and 32 GHz. a) 0° linearly polarized input (45° linearly polarized output). b) 45° linearly polarized input (90° linearly polarized output). c) 60° linearly polarized input (-75° linearly polarized output). d) 90° linearly polarized input (-45° linearly polarized output).

that the co-polarization's transmission magnitude is higher than 0.8 while the cross-polarization is less than 0.18 from 26 to 32 GHz (relative bandwidth of 21%). The co-pol and cross-pol transmission magnitudes under different polarized incident waves are shown in Figure 5d. The polarization is rotated 90° , and the transmission magnitudes are

nearly the same for other linearly polarized incident waves. The simulated vector E-field distributions for the meta-atom under 0° , 30° , 60° , and 90° linearly polarized incident waves are given in Figure 6. The polarization of all the input waves is observed to be rotated 90° after transmitting through the meta-atom.

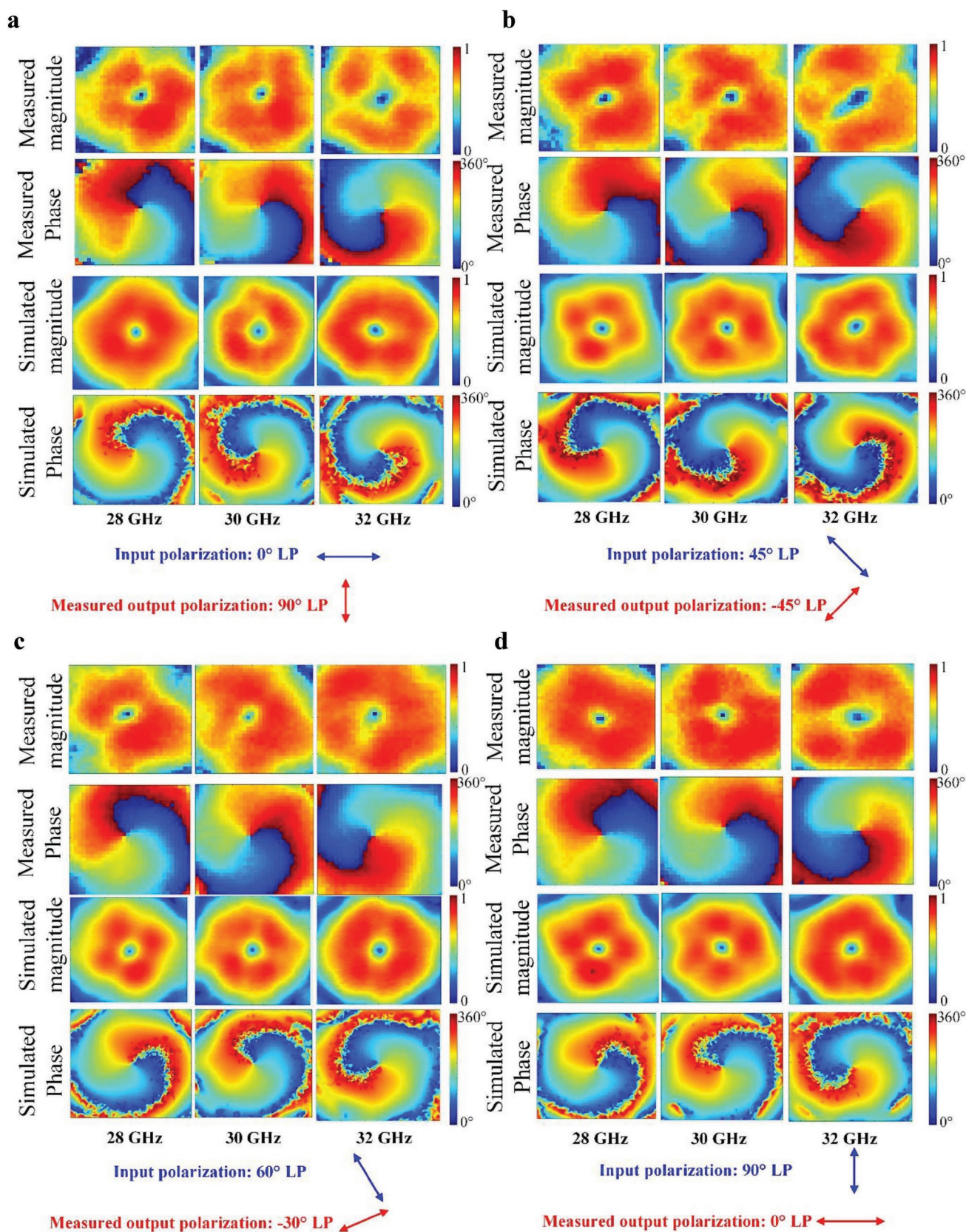


Figure 9. Simulated and measured near-field intensity and phase profile of the 90° polarization conversion MS. a) 0° linearly polarized input. b) 45° linearly polarized input. c) 60° linearly polarized input. d) 90° linearly polarized input.

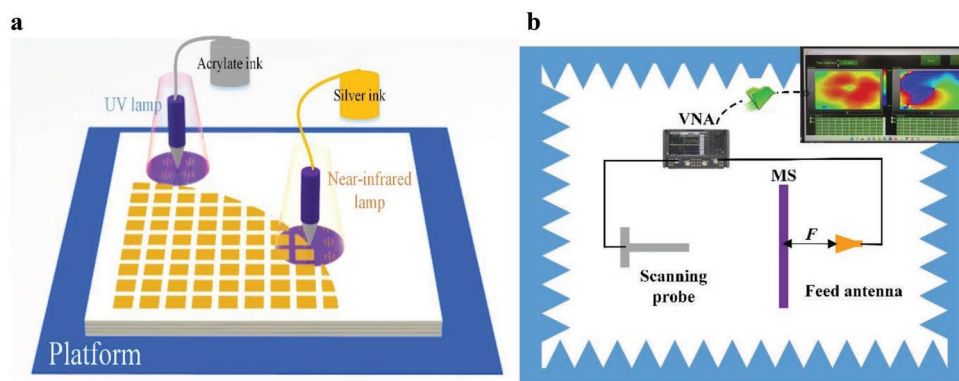


Figure 10. a) The multi-materials-integrated additive manufacturing technique for the sample fabrication. b) Schematic of the near-field measurement setup.

3. Results

Two different MSs are implemented based on the meta-atoms in Section 2 to demonstrate the arbitrary polarization conversion and wavefront shaping feature. The first polarization-insensitive MS achieves 45° polarization conversion with anomalous refraction. The compensating phase of each pixel on the MS's aperture is calculated using

$$\varphi(x, y) = -k_0 \sin \theta_b \times (x \cos \phi_b + y \sin \phi_b) + (\sqrt{x^2 + y^2 + F^2} - F) \times k_0 \quad (6)$$

where k_0 is the free-space wavenumber. θ_b and ϕ_b represent the angles in the elevation and azimuth planes, respectively. F is the focal length. WR-28 waveguide is used as the source and the corresponding focal length is set as 30 mm. 144 elements in total are used to form the MS with an aperture size of $47 \text{ mm} \times 47 \text{ mm}$. The design deflected the collimated beam at an angle of 15° in the design. The top, bottom, and internal views of the printed prototype are shown in **Figure 7**. The MS's radiation performance is measured in a far-field mm-wave chamber. The far-field radiation patterns of the co-polarization and cross-polarization under 0° , 45° , 60° , and 90° linear input are measured in the chamber by rotating the source feed (WR-28 waveguide) and the corresponding receiving horn antenna, as shown in **Figures 8a**, **8b**, **8c**, and **8d**, respectively. As can be seen, the beam is collimated and deflected at the same angle regardless of the polarization of the input. Meanwhile, the output co-polarization is rotated at an angle of 45° compared to the co-polarization of the waveguide source. The second MS is designed to achieve 90° polarization conversion with a collimated beam carrying OAM (topological charge $l = 1$). The compensating phase of the MS can be calculated using

$$\varphi(x, y) = (\sqrt{x^2 + y^2 + F^2} - F) \times k_0 + l \times \arctan\left(\frac{y}{x}\right) \quad (7)$$

The simulated and measured near-field magnitude and phase under 0° , 45° , 60° , and 90° linear polarizations are shown in **Figure 9**. The donut-like intensity and spiral-phase profile can be clearly observed in the simulated and measured results. The wavefronts are stable under different linearly polarized inputs, demonstrating the polarization-insensitive feature. In

addition, the polarization of the output is rotated 90° compared with that of the input. The simulated E-field/vector E-field for the two MSs is provided in **Figure S3**, Supporting Information, for better observing the polarization conversion and the wavefront shaping.

4. Conclusion

Ultrathin polarization-insensitive broadband MSs have been demonstrated for arbitrary linear polarization conversion and wavefront shaping. The phase delay-line connecting the receiving and the transmitting antenna provides 2π phase shifting for wavefront shaping. The rotation of the transmitting antenna provides the required polarization conversion for arbitrary linearly polarized input. Two polarization-insensitive MSs with different polarization conversion angles and wavefronts are conveniently fabricated and experimentally verified in the millimeter-wave region using advanced additive manufacturing. The simulated and measured results agree well. Under different linearly polarized incident waves, the performance of the MSs is very stable.

5. Experimental Section

The multi-materials-integrated additive manufacturing technique was used for sample fabrication. As shown in **Figure 10a**, the conductor and dielectric layers were implemented using silver nanoparticles and acrylate inks, respectively. A 395 nm UV lamp and a 0.75–1.4 μm near-infrared radiation (NIR) lamp were used to sinter the conductive inks and silver ink, respectively. Both vias and conductors were printed using the silver nanoparticle ink. The conductivity of the silver ink is $2 \times 10^7 \text{ S m}^{-1}$. In the printing process, no dielectric ink was jetted in the position of the vias and conductor layers. Instead, these vias and conductor layer positions were left for silver nanoparticle ink to fill. Compared with PCB fabrication, there were several advantages of using additive manufacturing for fabricating MS. First, the distance of adjacent conductor layers had to follow the laminate's standard thickness in PCB fabrication. However, the distance between adjacent conductor layers could be flexibly selected in additive manufacturing, providing designers with more design flexibility than the traditional multilayer PCB solutions. Second, a thin bonding layer must be used to bond different laminates in PCB solution, whereas no bonding process was required in additive manufacturing. The MS was built

in an additive way with robust connection and no post-processing procedure. Third, the additive manufacturing cost did not increase with the increase of the conductor layers, whereas the cost would be one of the issues in PCB if plenty of layers were used. The near-field measurement setup is shown in Figure 10b. The scanning probe was located 50 mm away from the MS and the scanning area was 70 mm × 70 mm. A vector network analyzer (VNA) could directly record the power and phase.

Supporting Information

Supporting Information is available from the Wiley Online Library or from the author.

Acknowledgements

The authors thank Mr. Minoru Yamada and the R&D team at Nano Dimension Hong Kong for technical support and fabrications. Special thanks to Jingyu Lin, Jizhe Liu, Majid Amiri, and Kevin Sharp for their assistance during the MS measurement.

Open access publishing facilitated by University of Technology Sydney, as part of the Wiley - University of Technology Sydney agreement via the Council of Australian University Librarians.

Conflict of Interest

The authors declare no conflict of interest.

Data Availability Statement

The data that support the findings of this study are available from the corresponding author upon reasonable request.

Keywords

additive manufacturing, metasurfaces, orbital angular momentum, polarization conversion, polarization insensitive, wavefront manipulation

Received: April 21, 2022

Revised: June 12, 2022

Published online: August 8, 2022

- [1] F. Aieta, M. Kats, P. Genevet, F. Capasso, *Science* **2015**, *347*, 1342.
- [2] A. Díaz-Rubio, V. Asadchy, A. Elsakka, S. A. Tretyakov, *Sci. Adv.* **2017**, *3*, e1602714.
- [3] C. Huang, C. Zhang, J. Yang, B. Sun, B. Zhao, X. Luo, *Adv. Opt. Mater.* **2017**, *5*, 1700485.
- [4] K. Zhang, Y. Yuan, X. Ding, B. Ratni, S. N. Burokur, Q. Wu, *ACS Appl. Mater. Interfaces* **2019**, *11*, 28423.
- [5] M. R. Akram, M. Q. Mehmood, X. Bai, R. Jin, M. Premaratne, W. Zhu, *Adv. Opt. Mater.* **2019**, *7*, 1801628.
- [6] A. K. Azad, A. V. Efimov, S. Ghosh, J. Singleton, A. J. Taylor, H.-T. Chen, *Appl. Phys. Lett.* **2017**, *110*, 224101.
- [7] Y. Yuan, K. Zhang, X. Ding, B. Ratni, S. N. Burokur, Q. Wu, *Photonics Res.* **2019**, *7*, 80.
- [8] J. Zhu, Y. Yang, M. Li, D. McGloin, S. Liao, J. Nulman, F. Iacopi, *IEEE Trans. Antennas Propag.* **2021**, *69*, 6261.
- [9] F. Aieta, P. Genevet, M. Kats, F. Capasso, *Opt. Express* **2013**, *21*, 31530.
- [10] M. F. Farahani, H. Mosallaei, *Opt. Lett.* **2013**, *38*, 462.
- [11] S. R. Biswas, C. E. Gutiérrez, A. Nemilentsau, I.-H. Lee, S.-H. Oh, P. Avouris, T. Low, *Phys. Rev. Appl.* **2018**, *9*, 034021.
- [12] T. Cai, G. M. Wang, F. X. Zhang, J. G. Liang, Y. Q. Zhuang, D. Liu, H. X. Xu, *IEEE Trans. Antennas Propag.* **2015**, *63*, 5629.
- [13] R. C. Zhu, Z. T. Zhang, J. F. Wang, C. L. Xu, S. Sui, X. F. Wang, T. H. Liu, Y. Zhu, L. Zhang, J. Wang, S. B. Qu, *Opt. Express* **2021**, *29*, 20150.
- [14] S. Y. Wang, J. D. Bi, W. Liu, G. Y. Wen, S. Gao, *IEEE Trans. Antennas Propag.* **2021**, *69*, 4670.
- [15] H. Zhang, X. Sha, Q. Chen, J. Cheng, Z. Ji, Q. Song, S. H. Yu, S. Xiao, *Adv. Mater.* **2022**, *34*, 2109255.
- [16] M. Q. Mehmood, S. Mei, S. Hussain, K. Huang, S. Y. Siew, L. Zhang, T. Zhang, X. Ling, H. Liu, J. Teng, A. Danner, S. Zhang, C. W. Qiu, *Adv. Mater.* **2016**, *28*, 2533.
- [17] G. Ding, K. Chen, X. Luo, J. Zhao, T. Jiang, Y. Feng, *Phys. Rev. Appl.* **2019**, *11*, 044043.
- [18] M. Piccardo, A. Ambrosio, *Nanophotonics* **2021**, *10*, 727.
- [19] J. Zhu, Y. Yang, N. Hu, S. Liao, J. Nulman, *ACS Appl. Mater. Interfaces* **2021**, *13*, 59460.
- [20] Y. Ming, Y. Intaravanne, H. Ahmed, M. Kenny, Y. Q. Lu, X. Chen, *Adv. Mater.* **2022**, *34*, 2109714.
- [21] I. Kim, W.-S. Kim, K. Kim, M. A. Ansari, M. Q. Mehmood, T. Badloe, Y. Kim, J. Gwak, H. Lee, Y.-K. Kim, *Sci. Adv.* **2021**, *7*, eabe9943.
- [22] P. Georgi, Q. Wei, B. Sain, C. Schlickriede, Y. Wang, L. Huang, T. Zentgraf, *Sci. Adv.* **2021**, *7*, f9718.
- [23] I. Kim, J. Jang, G. Kim, J. Lee, T. Badloe, J. Mun, J. Rho, *Nat. Commun.* **2021**, *12*, 3614.
- [24] G. Y. Liu, L. Li, J. Q. Han, H. X. Liu, X. H. Gao, Y. Shi, T. J. Cui, *ACS Appl. Mater. Interfaces* **2020**, *12*, 23554.
- [25] T. J. Cui, M. Q. Qi, X. Wan, J. Zhao, Q. Cheng, *Light: Sci. Appl.* **2014**, *3*, e218.
- [26] X. Zhang, W. Jiang, H. Jiang, Q. Wang, H. Tian, L. Bai, Z. Luo, S. Sun, Y. Luo, C. Qiu, T. Cui, *Nat. Electron.* **2020**, *3*, 165.
- [27] H.-X. Xu, G. Hu, M. Jiang, Y. W. S. Tang, Z. Wang, Y. Huang, X. Ling, H. Liu, J. Zhou, *Adv. Mater. Technol.* **2019**, *5*, 1900710.
- [28] Z. X. Wang, J. W. Wu, L. W. Wu, Y. Gou, H. F. Ma, Q. Cheng, T. J. Cui, *Adv. Opt. Mater.* **2021**, *9*, 2001609.
- [29] H.-X. Xu, L. Han, Y. Li, Y. Sun, J. Zhao, S. Zhang, C.-W. Qiu, *ACS Photonics* **2019**, *6*, 211.
- [30] Y. Li, X. Li, L. Chen, M. Pu, J. Jin, M. Hong, X. Luo, *Adv. Opt. Mater.* **2016**, *5*, 1600502.
- [31] Y. Xu, Q. Li, X. Zhang, M. Wei, Q. Xu, Q. Wang, H. Zhang, W. Zhang, C. Hu, Z. Zhang, *ACS Photonics* **2019**, *6*, 2933.
- [32] H.-X. Xu, G. Hu, Y. Wang, C. Wang, M. Wang, S. Wang, Y. J. Huang, P. Genevet, W. Huang, C. W. Qiu, *Light: Sci. Appl.* **2021**, *10*, 75.
- [33] H.-X. Xu, Y. Wang, C. Wang, M. Wang, S. Wang, F. Ding, Y. J. Huang, X. K. Zhang, H. W. Liu, X. H. Ling, W. Huang, *Research* **2021**, *2021*, 6382172.
- [34] K. E. Chong, L. Wang, I. Staude, A. R. James, J. Dominguez, S. Liu, G. S. Subramania, M. Decker, D. N. Neshev, I. Brener, Y. S. Kivshar, *ACS Photonics* **2016**, *3*, 514.
- [35] K. Ou, G. Li, T. Li, H. Yang, F. Yu, J. Chen, Z. Zhao, G. Cao, X. Chen, W. Lu, *Nanoscale* **2018**, *10*, 19154.
- [36] E. Arbabi, A. Arbabi, S. M. Kamali, Y. Horie, A. Faraon, *Optica* **2016**, *3*, 628.
- [37] M. Niroo Jazi, M. R. Chaharmir, J. Shaker, A. R. Sebak, *IEEE Trans. Antennas Propag.* **2015**, *64*, 99.
- [38] M. R. Akram, M. Q. Mehmood, T. Tauqeer, A. S. Rana, I. D. Rukhlenko, W. Zhu, *Opt. Express* **2019**, *27*, 9467.
- [39] S. Gao, C.-S. Park, S.-S. Lee, D.-Y. Choi, *Nanoscale* **2019**, *11*, 4083.
- [40] J. Li, C. Zheng, J. Li, G. Wang, J. Liu, Z. Yue, X. R. Hao, Y. Yang, F. Y. Li, T. T. Tang, Y. T. Zhang, Y. Zhang, J. Yao, *Photonics Res.* **2021**, *9*, 1939.

- [41] A. Paolini, S. Kollmannsberger, E. Rank, *Addit. Manuf.* **2019**, *30*, 100894.
- [42] Z. Jiang, Q. Liang, Z. Li, P. Lv, T. Chen, D. Li, *Adv. Opt. Mater.* **2019**, *7*, 1900475.
- [43] H. Yin, Q. Liang, Y. Duan, J. Fan, Z. Li, *Adv. Mater. Technol.* **2022**, *7*, 2101479.
- [44] A. Allam, K. Sabra, A. Erturk, *Phys. Rev. Appl.* **2020**, *13*, 064064.
- [45] S. Zhang, R. K. Arya, W. G. Whittow, D. Cadman, R. Mittra, J. C. Vardaxoglou, *IEEE Trans. Antennas Propag.* **2020**, *69*, 3788.
- [46] J. Zhu, Y. Yang, D. McGloin, S. Liao, Q. Xue, *IEEE Trans. Terahertz Sci. Technol.* **2021**, *11*, 433.
- [47] F. Zhou, W. Cao, B. Dong, T. Reissman, W. Zhang, C. Sun, *Adv. Opt. Mater.* **2016**, *4*, 1034.
- [48] Y. P. Zhang, J. J. Wang, *IEEE Trans. Antennas Propag.* **2006**, *54*, 1092.
- [49] Z. Shi, A. Y. Zhu, Z. Li, Y.-W. Huang, W. T. Chen, C.-W. Qiu, F. Capasso, *Sci. Adv.* **2020**, *6*, aba3367.
- [50] N. K. Grady, J. E. Heyes, D. R. Chowdhury, Y. Zeng, M. T. Reiten, A. K. Azad, A. J. Taylor, D. A. R. Dalvit, H. T. Chen, *Science* **2013**, *340*, 1304.
- [51] Y. Ge, C. Lin, Y. Liu, *IEEE Trans. Antennas Propag.* **2018**, *66*, 5974.
- [52] C. Pfeiffer, A. Grbic, *IEEE Trans. Microwave Theory Tech.* **2013**, *61*, 4407.
- [53] J. Zhu, Y. Yang, D. McGloin, R. R. Unnithan, S. Li, S. Liao, Q. Xue, *IEEE Trans. Antennas Propag.* **2020**, *68*, 4332.
- [54] X. Gao, X. Han, W. P. Cao, H. O. Li, H. F. Ma, T. J. Cui, *IEEE Trans. Antennas Propag.* **2015**, *63*, 3522.
- [55] J. Xu, R. Li, S. Wang, T. Han, *Opt. Express* **2018**, *26*, 26235.
- [56] K. Roy, R. Sinha, C. Barde, *Frequenz* **2022**, <https://doi.org/10.1515/freq-2021-0204>.
- [57] M. I. Khan, Z. Khalid, F. A. Tahir, *Sci. Rep.* **2019**, *9*, 4552.